



# Vortex dynamics impact on the wake flow of a marine rudder with leading-edge tubercles

Moritz Troll<sup>1</sup> · Weichao Shi<sup>1</sup> · Callum Stark<sup>1</sup> · Mehmet Atlar<sup>1</sup>

Received: 27 April 2022 / Accepted: 22 September 2022  
© The Author(s) 2022

## Abstract

The impact of two tubercle leading-edge (TLE) modifications on the turbulent wake of a reference marine rudder at Reynolds number  $2.26 \times 10^6$  was analysed numerically using Detached Eddy Simulations (DES). This paper studies the counter-rotating vortex pair formation around the TLE and their impact on the wake structures behind the rudder to find out if the vortex interaction can accelerate the tip vortex dissipation. According to the results, the tubercles enhanced lift for angles of attack (AOA)  $10^\circ$  and above, but at the cost of a drag penalty which reduced the rudders' lift-to-drag ratio. The formation of the distinctive stream-wise counter-rotating vortex pairs occurred behind the tubercles, which then interacted with the dominant tip vortex. Due to the inherent spanwise flow component of finite-span lifting surfaces the counter-rotating vortex pairs were generated at unequal strength and soon merged into singular vortices co-rotating with the tip vortex. The vortices facilitated flow compartmentalisation over the rudder suction side which broke up the trailing-edge vortex sheet and confined the spanwise flow separation over the rudder surface as AOA increased. The tubercles confined flow separation closer to the rudder tip which reduced the lift generation in the tip area and minimised the initial tip vortex strength. Large elements of stream-wise counter-rotating vorticity formed around the localised stall cells of the TLE rudders that interacted with the tip vortex downstream, introducing elliptical instabilities further weakening the tip vortex and changing its trajectory.

**Keywords** Rudders · Biomimetic design · Leading-edge tubercles · Computational fluid dynamics · Tip vortex · Vortex interaction

## List of symbols

$A$	Tubercle amplitude [m]	$N_i$	Mesh cell count [-]
$A_{\text{lift}}$	Lifting area [m <sup>2</sup> ]	$R_n$	Reynolds number [-]
$C_D$	Drag coefficient [-]	$S$	Span [m]
$C_L$	Lift coefficient [-]	$T_n$	N <sup>th</sup> tubercle trough [-]
$C_{L\text{max}}$	Maximum lift coefficient [-]	$V$	Free stream velocity [m s <sup>-1</sup> ]
$C_n$	N <sup>th</sup> tubercle crest [-]	$V_{\text{max}}$	Maximum velocity [m s <sup>-1</sup> ]
$C_{\text{nom}}$	Nominal chord length [m]	$y^+$	Non-dimensional distance from the wall to first mesh node [-]
$C_P$	Pressure coefficient [-]	$y_{\text{avg}}^+$	Average value of $y^+$ [-]
$D$	Drag force [N]	$y_{\text{max}}^+$	Maximum value of $y^+$ [-]
$L$	Lift force [N]	$\alpha$	Angle of attack [deg.]
$L_{\text{domain}}$	Length of the computational domain [m]	$\alpha_{\text{stall}}$	Stall angle [deg.]
$M_{11}$	11.3 Million cell mesh [-]	$\Delta t$	Time step [s]
$M_{21}$	21.6 Million cell mesh [-]	$\Delta_0$	Smallest grid cell length [m]
		$\lambda$	Tubercle wavelength [m]
		$\Omega$	Quarter chord sweep angle [deg.]
		$\rho$	Fluid density [kg m <sup>-3</sup> ]
		$\varphi$	Critical simulation variable [

✉ Weichao Shi  
weichao.shi@strath.ac.uk

<sup>1</sup> Department of Naval Architecture, Ocean and Marine Engineering, University of Strathclyde, Henry Dyre Building, 100 Montrose Street, Glasgow G4 0LZ, UK

## Abbreviations

AR	Aspect Ratio
AOA	Angle of Attack
CFD	Computational Fluid Dynamics
DES	Detached-Eddy Simulation(s)
EFD	Experimental Fluid Dynamics
GCI	Grid Convergence Index
LE	Leading Edge
LES	Large-Eddy Simulation(s)
MAE	Mean Absolute Error
MCS	Marine Control Surface(s)
RANS	Reynolds-Averaged Navier–Stokes Equations
SA	Spalart-Allamaras
SLE	Straight Leading Edge
SST	Shear Stress Transport
TE	Trailing Edge
TKE	Turbulent Kinetic Energy
TLE	Tubercle Leading Edge

## 1 Introduction

Turbulence remains one of the last unsolved phenomena in modern fluid dynamics. Every time when an object is placed into a fluid flow it will interact with the fluid generating chaotic particle motions, commonly referred to as turbulence. Marine control surfaces (MCS), such as rudders, fin stabilisers, or submarine hydroplanes are no exemption from this.

MCS typically are foil-shaped appendages used as primary steering devices for modern surface ships and submarines (Molland and Turnock 2007). They are designed for effectiveness given by the amount of lift that can be generated and for efficiency, reflected in the lift-to-drag ratio (Liu and Hekkenberg 2017). Whilst providing useful lifting forces when deflected, the control surfaces cause disturbances to the flow and a turbulent wake is created as a by-product. Two key elements of this turbulent wake are the flow separation on the suction side surface when the boundary layer begins to detach and the distinctive tip vortex that is generated when the pressure differences between control surface sides are balanced out over the tip section (Molland and Turnock 2007).

Whilst turbulence is inevitable, there are numerous adverse effects from the turbulent wake detrimental to a ship's performance. Turbulence dissipates energy and therefore increases drag. The dissipated energy is converted to heat, increasing the non-acoustic wake signatures detrimental to naval vessels, and especially submarines. The vortex shedding due to boundary layer separation can also inflict structural vibrations increasing material fatigue and noise. The tip vortices are highly turbulent and slow-decaying flow structures. Their low-pressure core may give rise to cavitation causing flow noise. They can also have adverse effects on

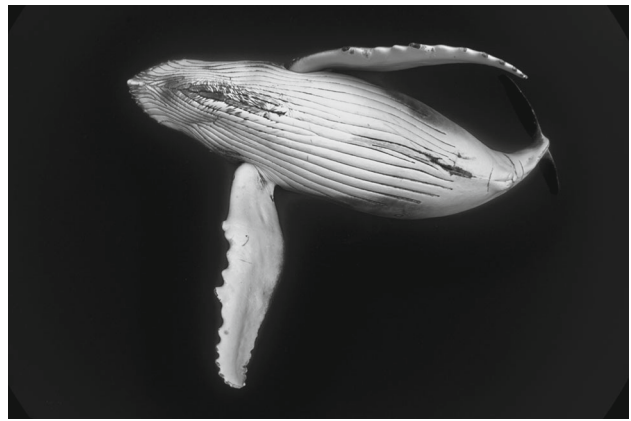


**Fig. 1** Leading-edge tubercles as seen on a humpback whale pectoral flipper (©Grant Thomas)

structures located in the downstream wake such as propulsors, and their long persistence in the flow makes them a critical part of the non-acoustic wake. The significance of the control surface tip vortex structures within the overall wake of a submarine is evident from the flow visualisations of the Joubert BB2 submarine presented in Carrica et al. (2019).

In the constant strive to develop MCS that generate higher lift forces, reduced drag forces, and prolong flow attachment to increase the stall angle, researchers recently started drawing inspiration from humpback whales (*Megaptera novaeangliae*). Humpback whales have superior agility amongst baleen whales, which has been attributed to distinctive bumps along their leading edge (LE), the so-called tubercles, as shown in Fig. 1.

The tubercle leading edge (TLE) is a passive flow control device that gives the flippers a unique flow profile that prolongs flow attachment, delays stall, and increases post-stall lift (Fish and Battle 1995; Miklosovic et al. 2007, 2004). Finite span hydro/aerofoils respond particularly well to the addition of TLE. Lift enhancements have been reported in the pre-stall regime, and despite the maximum lift coefficient being reduced, there is a more gradual stall behaviour with significant improvements in the post-stall lift (Custodio et al. 2015; Miklosovic et al. 2007, 2004; Stanway 2008; Weber et al. 2010). Several experimental studies on low aspect ratio (AR) marine rudders with TLE using NACA foil sections were conducted. NACA sections are part of a large series of aerofoil profiles developed and experimentally tested by the National Advisory Committee for Aeronautics (NACA). Weber et al. (2010) analysed a rudder with NACA 0016 section, Shanmukha Srinivas et al. (2018) one with NACA 0018 section, with both studies reporting benefits from tubercles in the post-stall regime. In addition, a numerical analysis for marine rudders with NACA 0020 section that had different tubercle coverage along the LE conducted by Yoon et al. (2011) also reported superior post-stall performance.

Not only does the TLE provide a means of increasing the lifting performance of hydrofoils, but it also has the potential to alter and minimise the turbulent wake generation. To understand how this can be achieved, the flow mechanisms behind the TLE need to be explained. When the free stream approaches the LE it is diverted into the troughs between adjacent tubercles and a pair of stream-wise counter-rotating vortices begin to form that stream over the foil suction side. These vortices exchange momentum within the boundary layer, energise the flow over the tubercle crests and confine separation to the tubercle troughs, thereby smoothing and delaying flow stall (Fish et al. 2008; Malipeddi et al. 2012; Pedro and Kobayashi 2008; Rostamzadeh et al. 2017). The effect of the tubercle vortices has been compared to that of wing fences which minimise spanwise flow and confine flow separation to small localised stall cells, preventing the rapid spread of flow separation (Bolzon et al. 2015; Pedro and Kobayashi 2008).

Finite span (3D) foils in particular experience performance degradation due to spanwise flow components in several ways: a downwash forms which generates induced drag; Net pressure differences having to be cancelled out over the foil tip result in the formation of distinctive, slow-decaying tip vortices (Molland and Turnock 2007); The tip vortices themselves dissipate further energy increasing drag; Lastly, their low-pressure core can cause cavitation inception (Knister et al. 2020) resulting in further performance degradation, increased flow noise, and material erosion (Liu and Hekkenberg 2017). The TLE can positively influence all these problems. Johari (2015) and Weber et al. (2010) reported very different cavitation behaviour for rudders fitted with TLE compared to their reference counterparts with sheet cavitation contained in between tubercle troughs in both studies and the tip vortex cavitation diminishing at lower AOA in the former and inception being delayed to higher AOA in the latter study. Stark et al. (2021) reported a similar “cavitation funnel effect” for TLE applied to a ducted marine propeller. Shi et al. (2016) showed diminishing effects on the tip vortex strength and the associated cavitation for a tidal turbine blade with TLE. The “wing fence effect” of the tubercles furthermore has the potential to reduce induced drag through minimising spanwise flow, as well as reducing the tip vortex build-up. Tip vortex strength, size, decay, and trajectory may be further influenced through vortex interaction between the tip vortex and the tubercle vortices.

Bolzon et al. (2017) assessed the impact of a single tubercle at the tip of a swept foil. Their study found that for a peak configuration of the tip tubercle, the tip vortex strength was increased, whereas the tubercle vortex closest to the tip in a trough configuration reduced the tip vortex strength. Custodio (2012) on the other hand reported that for angles of attack (AOA) post-stall, the tip vortex strength downstream of a tubercle foil increased. This however was attributed to the

overall increase in lift from the tubercles. A recent study by Loughnane et al. (2021) experimentally analysed the impact of LE undulations applied to a NACA 0012 aerofoil on the wing tip vortex in a low-speed wind tunnel. Their study showed that undulated LE reduces the tip vortex circulation for a given lift coefficient by up to 25%, and furthermore, their study also reported a reduction in induced drag for the modified aerofoils (Loughnane et al. 2021). However, their study mainly stated the flow compartmentalisation by the tubercle vortices as a cause for reduced spanwise flow and a resulting reduction in induced drag and tip vortex circulation without considering potential interactions between the tubercle vortices and the tip vortex. The results from Custodio (2012) are contradictory to Shi et al. (2016), who reported a reduction in tip vortex strength whilst lift was maintained or even enhanced, which suggest that the presence of vortex interaction between the tubercle vortices and the tip vortex causing an accelerated breakdown of the tip vortex within the wake. This was shown in a study by Stark and Shi (2021) on the effect of TLE applied to a marine duct where a significant interaction between the tubercle vortices generated over the duct and the vortex system of the propeller occurred, which accelerated the breakdown of the blade tip vortex as well as reducing the overall turbulent kinetic energy levels within the wake. Bolzon et al. (2017) showed that if the tubercle vortex closest to the foil tip opposes the tip vortex rotational direction, the tip vortex is weakened.

Generally, if two vortices are streaming in parallel and within close enough distance for their respective strain fields to become overlapped, they will begin to interact with each other causing two-dimensional dynamics (merging) and three-dimensional instabilities (displacement from the original trajectory). Three-dimensional instabilities occur in the form of long-wave Crow instabilities, shortwave elliptical instabilities, or a combination of the two (Leweke et al. 2016). The TLE wake offers a great potential for various modes of vortex interaction between the tubercle vortices and the tip vortex, or the tubercle vortices amongst themselves. Knister et al. (2020) showed how the presence of a weak secondary vortex could lead to the break-up of a strong primary vortex of opposing sign.

The formation of stream-wise counter-rotating vortex pairs generated by tubercles has been widely reported, but to date studies on the generating mechanisms remain largely focussed on infinite span (2D) foils. Whilst several studies reported encouraging results on the reduction of tip vortex strength through the addition of TLE, the effect of the tubercle vortex pairs on the turbulent wake and their interaction with the tip vortex remain largely unstudied. This study aims to address the gaps in the literature regarding the formation mechanisms of the tubercle vortices for finite-span hydrofoils, focussing on their impact on the downstream turbulent wake structures. To achieve this, tubercle leading-edge

modifications will be applied to a benchmark marine rudder simulated in fully turbulent flow at a high Reynolds number ( $R_n$ ) using Computational Fluid Dynamics (CFD).

## 2 Reference rudder model and leading-edge modifications

### 2.1 All-movable rudder reference model

A reference rudder model as presented in Folger Whicker and Fehlner (1958) was replicated in this study to allow for experimental validation of the numerical model. This rudder model was chosen because it is representative of not only a typical marine rudder but also has a strong resemblance to a typical submarine diving plane, such as seen on the Joubert BB2 submarine model, where a reduction of tip vortex generation may be of particular interest.

The study provides results for this reference rudder for a high  $R_n$  of up to  $2.26 \times 10^6$  where the flow can be regarded as fully turbulent (Folger Whicker and Fehlner 1958). The reference rudder has a nominal chord length ( $C_{nom}$ ) of 0.61m, a span ( $S$ ) of 0.914m resulting in a geometric aspect ratio of 1.5, a quarter chord sweep angle ( $\Omega$ ) of  $11^\circ$ , a taper ratio of 0.45, and a rounded-off (semi-circular) tip. It has a NACA 0015 foil section. The planform definitions of the reference rudder are outlined in Fig. 2 below.

### 2.2 Tubercle design

Two TLE variations of fixed amplitude with two different wavelengths were designed. The tubercles were modelled as a sine function that was subsequently superimposed onto the linear function of the unmodified LE. The amplitude ( $A$ ) was fixed at  $5.0\% C_{nom}$ , which was the best performing amplitude during preliminary analysis. The wavelengths ( $\lambda$ ) of the two designs were set to  $21\% C_{nom}$  and  $36\% C_{nom}$  which resulted in  $4^{1/4}$  and  $7^{1/4}$  tubercles, respectively. The  $1/4$  tubercle arises from the LE modification being designed to terminate on a tubercle crest, to produce tubercle vorticity opposing the tip vortex rotational direction from the tubercle closest to the rudder tip, as proposed by Bolzon et al. (2017). The three different rudder designs are hereinafter referred to as SLE for the straight leading-edge reference model, TLE4 for the  $4^{1/4}$  tubercle model, and TLE7 for the  $7^{1/4}$  tubercle model. The three models can be seen in Fig. 3.

## 3 Numerical setup

### 3.1 Numerical model

Analyses were carried out using the commercial Computational Fluid Dynamics (CFD) code STAR-CCM + . The

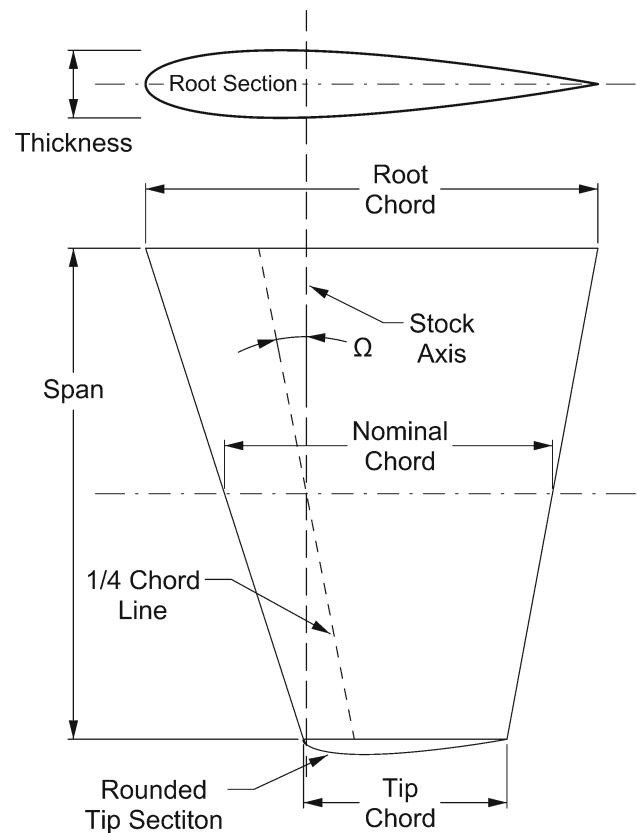


Fig. 2 Reference rudder planform definitions

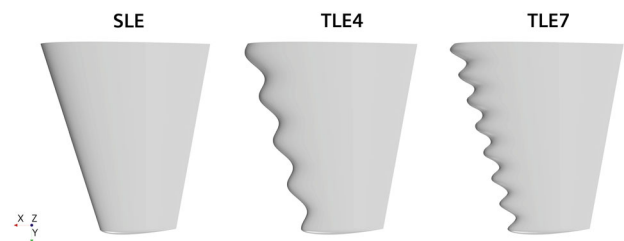


Fig. 3 Reference rudder (SLE), 4 tubercle rudder (TLE4), and 7 tubercle rudder (TLE7)

hydrodynamic flow field was solved using implicit unsteady incompressible Detached Eddy Simulations (DES). DES is a hybrid approach combining Large-Eddy Simulations (LES) to solve the main fluid domain, whilst Reynolds-Averaged Navier–Stokes (RANS) solvers are used to resolve the near-wall boundary layer flow regions. This approach is highly applicable to the hydrodynamic flow problems targeted in this study due to DES' superior capabilities in resolving the expected separated flow areas without excessive computational requirements. Furthermore, several researchers have already presented successful analyses of TLE applications using DES (Câmara and Sousa 2013; Malipeddi et al. 2012; Pedro and Kobayashi 2008).

The SIMPLE flow solver was employed with a hybrid second-order upwind/bounded-central differencing discretisation scheme. Analysing TLE modifications for an infinite span aerofoil in CFD, Malipeddi et al. (2012) reported the best results for the complex flows at high AOA using DES with the shear stress transport (SST)  $k-\omega$  model, whilst stating limitations for the Spalart-Allamaras (SA) model which did not reach convergence for higher AOA. Therefore, an approach using the Improved Delayed Detached Eddy Simulation (IDDES) solver with the SST  $k-\omega$  turbulence model was chosen. Implicit unsteady first-order temporal discretisation was used.

The reference rudder results were provided for  $R_n$   $2.26 \times 10^6$  based on nominal chord length, which equated to an inlet velocity of 4.408m/s. The time step ( $\Delta t$ ) was calculated following the guidelines by Spalart (2001) shown in Eq. (1)

$$\Delta t = \Delta_0 / V_{\max} \approx 0.001 \text{ s}, \quad (1)$$

where  $\Delta_0$  is the smallest grid cell length and  $V_{\max}$  is an estimate of the maximum velocity encountered within the flow regions of interest. The mean flow residence time at the target velocity was calculated by Eq. (2)

$$L_{\text{domain}} / V = 2.7 \text{ s}, \quad (2)$$

where  $L_{\text{domain}}$  is the length of the computational domain and  $V$  is the freestream velocity. To aid convergence a 2.0s linear velocity ramp from 0m/s to the target velocity of 4.408m/s was added at the inlet. Solution times were aimed to be twice the residence time after the velocity ramp for the flow to achieve statistical steadiness and to allow for time-averaged results to be taken. The resulting target physical simulation time was  $\sim 8.0$ s, although most simulations had stabilised for a period of time beforehand.

### 3.2 Computational domain and boundary conditions

A cuboid-shaped domain was created with the rudder placed vertically centred on the right-hand-side boundary (see Fig. 4). The coordinate origin was located at the rudder stock location on the root chord, with the  $x$ -axis in the upstream,  $y$ -axis in the span, and  $z$ -axis in the vertical direction. The velocity inlet was placed five chord lengths upstream, the pressure outlet 15 chord lengths downstream, the top, bottom, and left-hand-side boundaries were set to slip walls and placed at five chord lengths from the origin each.

### 3.3 Grid generation

The computational domain was meshed using polyhedral cells. The boundary layer was resolved using prism layers

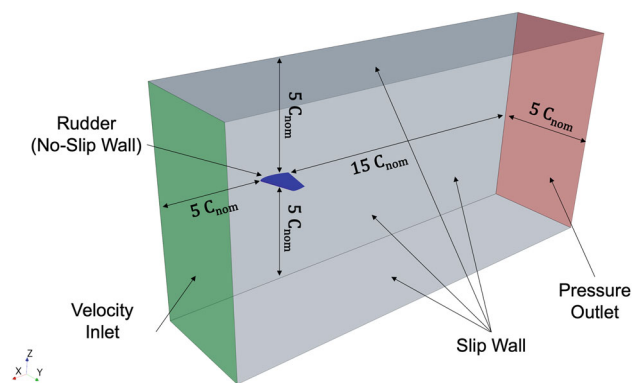


Fig. 4 Computational domain sizing and boundary conditions

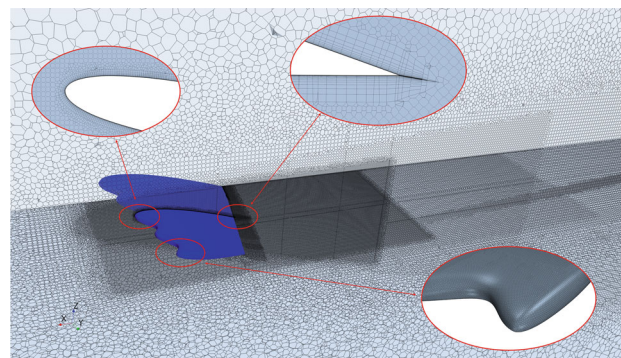
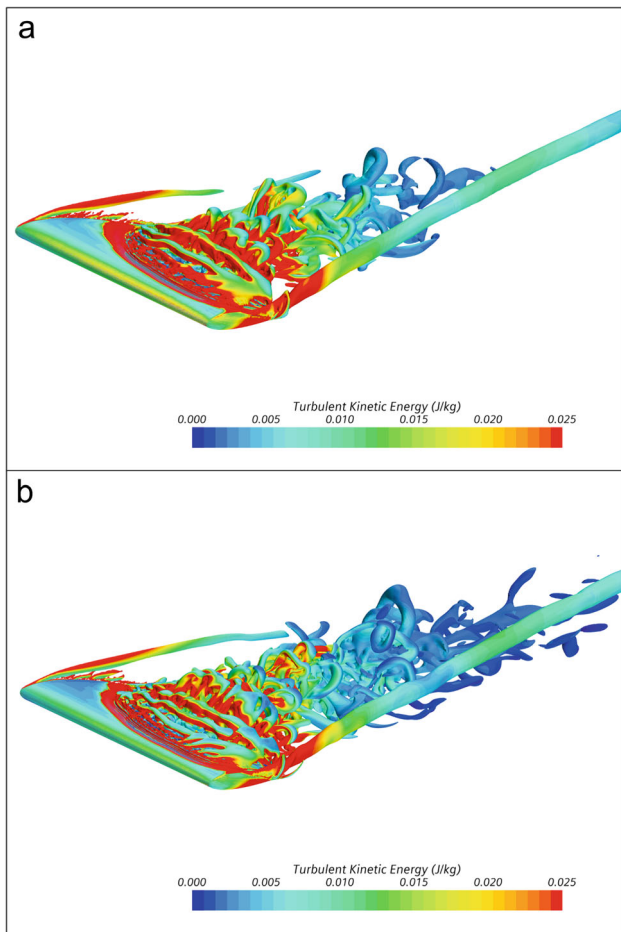


Fig. 5 Volume mesh of the computational domain

tailored for the low  $y^+$  wall treatment model with a target  $y^+ < 1$ . 18 prism layers were used, expanding with a growth rate of approximately 1.4. The prism layer mesh was extended onto an interface past the trailing edge (TE) into the core mesh; otherwise, it would have collapsed upstream on the surface due to the sharp TE angle, which would have affected the resolving of the boundary layer. The final mesh for the highest lifting (and resulting highest suction side velocity) test case achieved  $y_{\text{avg}}^+ \approx 0.68$  and a maximum  $y_{\text{max}}^+ \approx 2.5$  on the LE. The volume mesh for one representative case is displayed in Fig. 5.

The rudder surface was meshed in a uniform manner and with a resolution as fine as feasible within the computational limits to accurately resolve the boundary layer where most of the vorticity of the turbulent wake is generated. Several mesh refinements were added in the vicinity of the rudder and the downstream area to resolve the turbulent wake accurately. The tip vortex paths were estimated in preliminary simulations and additional refinements were added in its approximate trajectory, aiming to cover the vortex core diameter with at least 10 mesh cells.

An initial set of solutions was generated with an 11.3 million cell mesh ( $M_{11}$ ). This mesh however could only capture the chaotic separated wake structures with a limited resolution. With the tubercles producing complex flow



**Fig. 6** Comparison of the resolution of vortical wake structures through Q-Criterion displays for M11 (a) and M21 (b)

patterns through the generation of counter-rotating vortices and this study investigating the effects of these vortices on the downstream wake, a mesh is required capable of providing the highest possible resolution of small vortical structures within feasible computational limits. Therefore, a second, much more refined grid with 21.6 million cells ( $M_{21}$ ) was employed for stall and post-stall AOA, where the wake structures become particularly complex due to heavy flow separation. Figure 6 highlights the differences in resolution of the small vortical wake structures between  $M_{11}$  and  $M_{21}$  with Turbulent Kinetic Energy (TKE) plotted on a Q-Criterion iso-surface ( $Q = 100.0/s^2$ ) for the example case of AOA  $21.5^\circ$ . It can be seen how smaller wake elements are captured in the simulation and the downstream numerical diffusion of vortical structures is reduced.

### 3.4 Hydrodynamic validation against experimental reference study

The lift and drag results presented in the reference study by Folger Whicker and Fehlner (1958) were compared against

**Table 1** Test conditions for rudder models

Angle of attack	Test condition
$0^\circ$	Zero-lift condition
$5^\circ, 10^\circ, 15^\circ$	Linear lifting regime
$20^\circ$	Maximum lift condition
$21.5^\circ$	Stall of reference rudder
$25^\circ, 30^\circ$	Post-stall regime

the numerical results obtained for  $M_{11}$  and  $M_{21}$ . The results were presented in coefficient form with lift coefficient,  $C_L$ , and drag coefficient,  $C_D$ , defined as follows:

$$C_L = \frac{2L}{\rho V^2 A_{lift}}, \quad (3)$$

$$C_D = \frac{2D}{\rho V^2 A_{lift}}, \quad (4)$$

where  $L$  and  $D$  are the lift and drag forces respectively,  $\rho$  is the fluid density,  $V$  is the free stream velocity, and  $A_{lift}$  is the lifting area defined as  $S \times C_{nom} \cdot 8$  AOA over a large range were selected to cover the various flow regimes the rudder can experience during operation. The selected test conditions and their respective flow regime are outlined in Table 1. The validation results are shown in Fig. 7, where the presented numerical values are averages of the statistically steady simulations.

The numerical results for  $C_L$ ,  $C_D$ , and  $L/D$  are in good agreement with the experimental data, although  $C_{Lmax}$  is underpredicted.  $M_{11}$  failed to accurately predict flow separation at higher AOA, which was addressed through the introduction of the more refined  $M_{21}$  that accurately captured the separated wake structures. The results presented in the following section were generated with  $M_{11}$  for AOA  $0^\circ - 15^\circ$  and with  $M_{21}$  for AOA  $20^\circ - 30^\circ$ . The mean absolute error,  $MAE$ , for  $C_L$  and  $C_D$  was calculated as

$$MAE = \frac{\sum_{i=1}^n |C_{EFD,i} - C_{CFD,i}|}{n}, \quad (5)$$

where  $C_{EFD,i}$  is the representative force coefficient from the experimental reference study,  $C_{CFD,i}$  the force coefficient value from the numerical simulations, and  $n$  the total number of data samples. The resultant error values were  $MAE_{C_L} = 4.58\%$  and  $MAE_{C_D} = 0.44\%$ .

### 3.5 Grid convergence analysis

Additional verification is provided through a Grid Convergence Index (GCI) analysis as outlined in Celik et al. (2008). AOA  $10^\circ$  was chosen for pre-stall assessment for  $M_{11}$  and

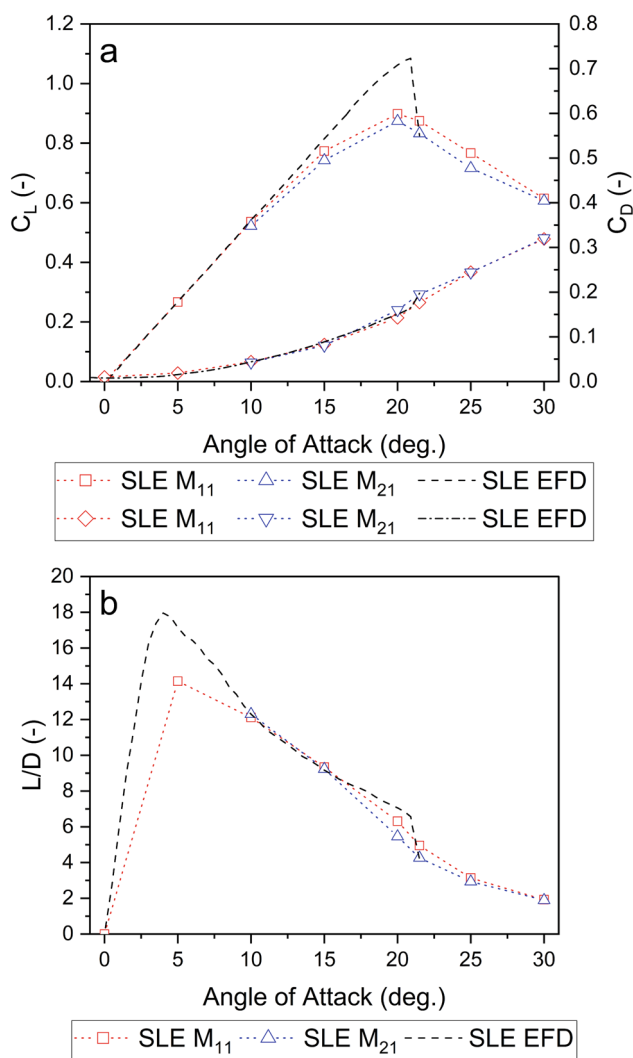


**Fig. 7** Validation of reference rudder force coefficients (a) and lift-to-drag ratio (b) for  $M_{11}$  and  $M_{21}$  against experimental results from Folger Whicker and Fehlner (1958) for  $R_n 2.26 \times 10^6$

AOA  $21.5^\circ$  for post-stall assessment for  $M_{21}$ . GCI is a method based on Richardson extrapolation and compares the results of a critical variable ( $\varphi$ ) for three progressively refined meshes ( $N_i$ ). The resultant GCI value states numerical uncertainty within the results progressing from a coarser

to the next finer mesh.  $C_L$  and  $C_D$  were chosen as critical variables. The results of the GCI study are presented in Table 2.  $M_{11}$  converged monotonic, and the GCI values for the fine grid of 1.5% and 2.1% were deemed sufficiently accurate. The convergence for the triplet of  $M_{21}$  is oscillatory, which further highlights the difficulties of numerical stall prediction. Whilst the GCI results for  $M_{21}$  are inconclusive, the numerical setup showed good agreement with the experimental results and with a MAE of under 5% it was deemed sufficiently accurate for the comparative analysis of the three rudder geometries.

## 4 Results and discussion

### 4.1 Force coefficient comparison

Force coefficients give a first indication of how the tubercle modifications affect the performance of the reference rudder. Figure 8 presents a comparison for the lift coefficient (8a), drag coefficient (8b) and their ratio (8c) for the three rudder models.

At AOA  $0^\circ$  and  $5^\circ$ , the rudders show no appreciable difference in performance coefficients. This changes as the AOA increases. At  $10^\circ$  the TLE rudders show opposite effects. TLE4 minimises  $C_L$  by 6%, whereas TLE7 increases it by 3%. For all AOA of  $15^\circ$  and above both TLE rudders improve lift, however, paired with a significant drag penalty from AOA  $20^\circ$  onwards causing a slight reduction in lift-to-drag ratio for the whole lift curve. Like the findings of previous researchers, the  $C_L$  improvements are most significant in the post-stall regime at AOA  $25^\circ$  and  $30^\circ$  with enhancements of 14% and 19%, respectively. Both TLE rudders show very similar post-stall lift, but TLE4 has a less significant drag penalty, making it the more favourable modification with respect to lifting performance. This is in line with the findings of Custodio et al. (2015); Weber et al. (2010), who reported that tubercles with larger wavelengths perform better for a fixed amplitude. The general improvements in  $C_L$  suggest that the rudder effectiveness is increased by the tubercles, whereas due to the reduction in lift-to-drag ratio, the modifications make the rudder less efficient.

**Table 2** Numerical uncertainty results for  $C_L$  and  $C_D$

AOA	$\varphi$	$\varphi_1$	$\varphi_2$	$\varphi_3$	$N_1$	$N_2$	$N_3$	GCI <sub>21</sub>	GCI <sub>32</sub>
$M_{11}$ $10.0^\circ$	$C_L$	0.537	0.540	0.545	11,300,000	4,400,000	2,000,000	1.47%	2.27%
	$C_D$	0.044	0.045	0.047	11,300,000	4,400,000	2,000,000	2.10%	4.72%
$M_{21}$ $21.5^\circ$	$C_L$	0.832	0.882	0.827	21,600,000	9,700,000	3,700,000	Oscillatory convergence	
	$C_D$	0.195	0.190	0.195	21,600,000	9,700,000	3,700,000	Oscillatory convergence	

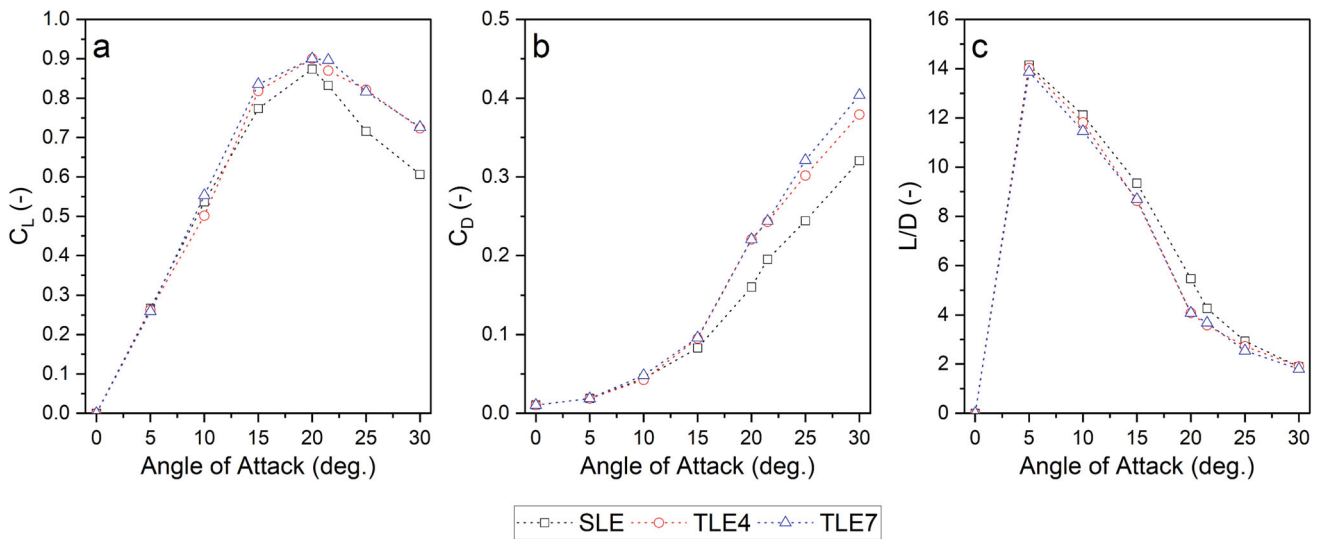


Fig. 8 Force coefficient comparison between SLE, TLE4, and TLE7 at  $R_n 2.26 \times 10^6$

### 4.2 Pressure coefficient comparison

The differences in lifting performance at the lower pre-stall angles of attack are better understood when investigating the pressure distributions over the rudder suction sides. Furthermore, some of the key principles that cause the formation of the stream-wise counter-rotating vortex pairs can also be explained. The pressure coefficient,  $C_p$ , was visualised on the rudder suction side surface (Figs. 9 and 10a–c) and plotted for representative foil sections at several spanwise positions

(Figs. 9 and 10d–f).  $C_p$  is defined as

$$C_p = \frac{2(P - P_0)}{\rho V^2}, \tag{6}$$

where  $P$  is the static pressure measured on the hydrofoil surface and  $P_0$  is the reference pressure upstream from the hydrofoil. The plotted measurement sections are indexed by their respective tubercle crest number,  $C_n$ , or trough number,  $T_n$ , from the root section outwards.

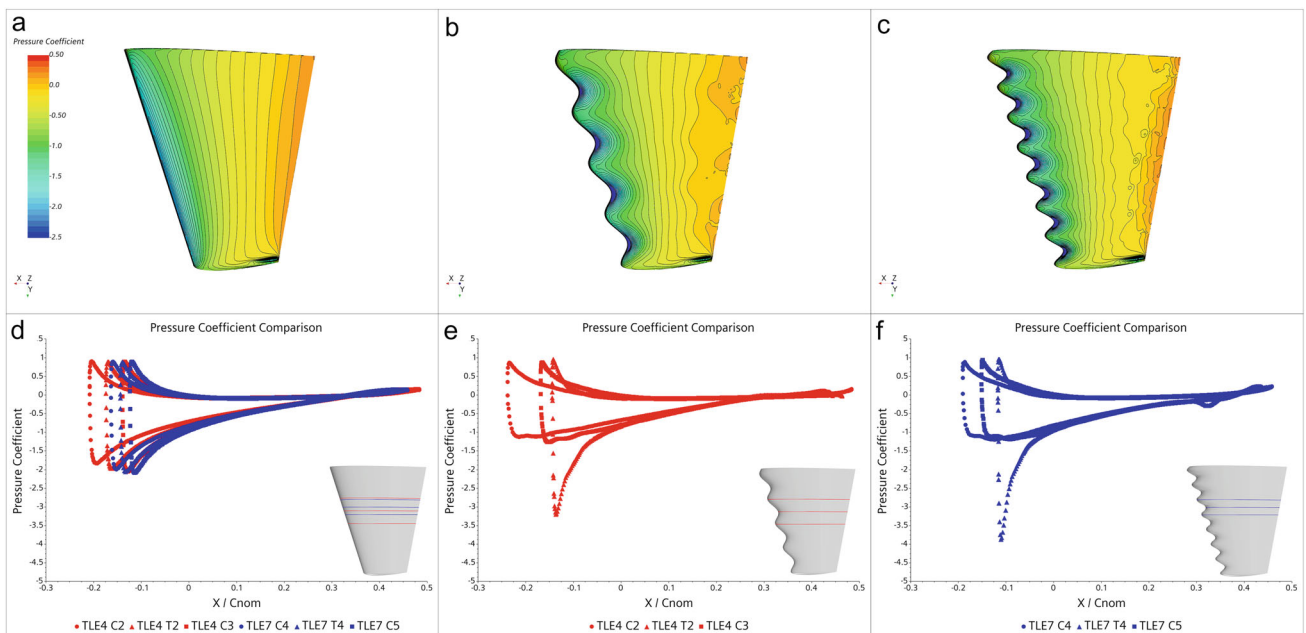
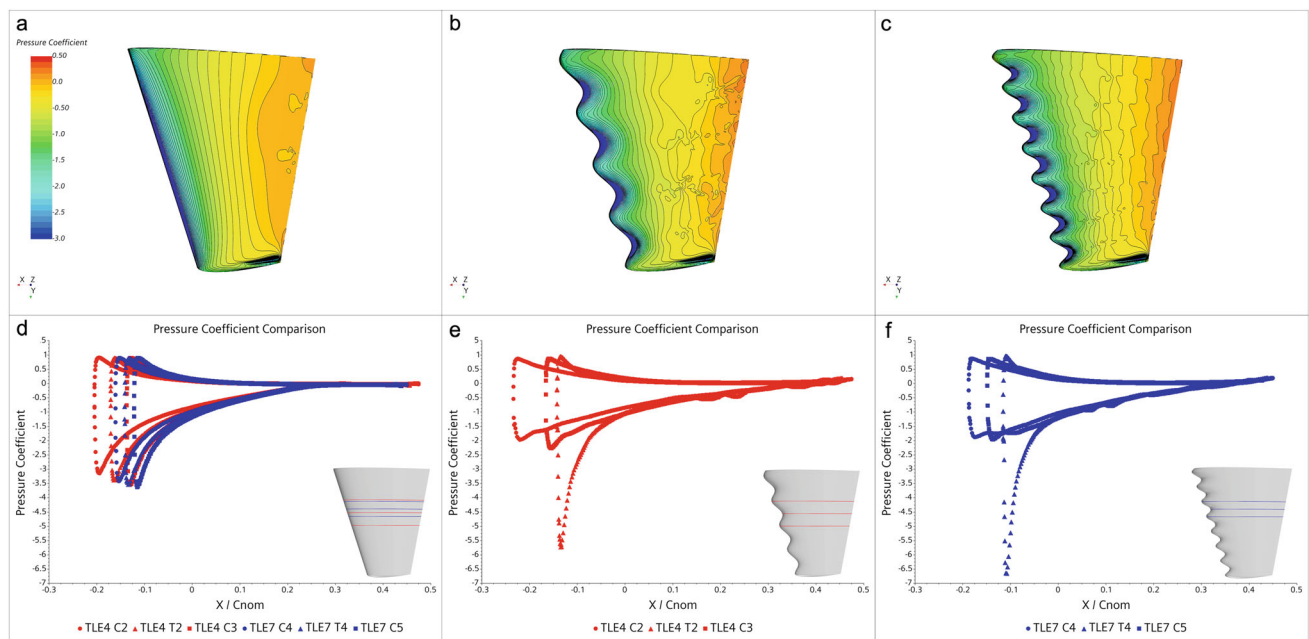


Fig. 9 Pressure coefficient distribution comparison between SLE (a, d), TLE4 (b, e), and TLE7 (c, f) at AOA 10° (pre-stall) for rudder suction side (top) and representative foil sections (bottom)



**Fig. 10** Pressure coefficient distribution comparison between SLE (a, d), TLE4 (b, e), and TLE7 (c, f) at AOA 15° (pre-stall) for rudder suction side (top) and representative foil sections (bottom)

When the flow approaches the leading edge, it is diverted into the troughs between adjacent tubercles and accelerates. As a result, low-pressure cells form in the tubercle troughs, which can be seen clearly in Fig. 9, and a pressure variation along the span is induced. The flow itself is forced around the tubercles, which has been reported to give rise to initial stream-wise counter-rotating vorticity (Rostamzadeh et al. 2014).

Due to the spanwise pressure variation, the TLE rudders exhibit an unconventional means of lift generation when compared to conventional hydrofoils, such as the SLE reference rudder. In Fig. 9e, f, it can be seen how a very pronounced low-pressure spike forms in the trough section, whilst the spike is reduced and smoothed over the crest sections. The same sections for the SLE rudder in Fig. 9d show a pressure distribution of a typical hydrofoil. They also exhibit a low-pressure spike near the leading edge but are less pronounced compared to the TLE trough sections, and all foil sections plotted follow a very similar shape.

The pronounced low-pressure spike for the TLE trough sections causes a local increase in adverse pressure gradient. This larger adverse pressure gradient, combined with the reduced chord length, leads to early flow separation downstream from the troughs where small, localised stall cells form. The opposite effect holds true for the crests, where the adverse pressure gradient is reduced compared to the trough section and reference rudder sections. The chord length is extended, so the flow attachment is prolonged. This becomes

visible in Fig. 10b, c, where the dark orange areas downstream from the troughs on the trailing edge show a positive pressure coefficient, representative of separated flow in the small stall cells.

The different lifting performance of the two TLE rudders may be explained when looking at the pressure coefficient variations in Fig. 9d–f. TLE7 (Fig. 9f) shows a strongly pronounced low-pressure peak for  $T_4$  and an increased net pressure difference for  $C_{4,5}$  compared to the SLE rudder, which across the whole rudder may have led to the 3% increase in  $C_L$ . TLE4, on the other hand, shows a less developed peak for  $T_2$  and a smaller net pressure difference over  $C_{2,3}$ . This suggests that at this AOA the larger tubercles are not producing counter-rotating vortices of sufficient strength yet, and therefore, the lifting performance is degraded when compared to the SLE rudder. Comparing the same sections at AOA 15° in Fig. 10d–f, the low-pressure peak of TLE4 has increased, along with the net pressure differences over the crest sections, which have become larger than their counterparts on the SLE rudder. TLE4 now generates more lift than SLE, too, but the effects are still stronger for TLE7.

The pressure contours for the SLE rudder (Fig. 10a) are very smooth and evenly spaced. The pressure contours for TLE4 and TLE7 (Fig. 10b, c), in contrast, show strong spanwise variations as previously mentioned that are maintained from the LE all the way to the TE. This supports the argument that flow compartmentalisation generated by the tubercles enables them to limit the spanwise progression of flow separation (Bolzon et al. 2015; Pedro and Kobayashi, 2008).

### 4.3 Streamwise counter-rotating vortex formation and near-field interaction

This section looks at the formation of the tubercle vortices themselves, their interaction with each other, and with the tip vortex, and how they affect the separated wake behind the rudder models in general. To analyse these flow dynamics, cut-planes normal to the free stream with scalar displays for stream-wise vorticity were defined. The cut planes are spaced evenly along the nominal chord in intervals of  $12.5\%C_{\text{nom}}$ . Additional 9 cut planes were added in the wake spaced evenly at  $25\%C_{\text{nom}}$  intervals downstream from the TE. Positive vorticity is rotating in the clockwise direction (coloured red), negative vorticity in the anti-clockwise direction (coloured blue) about the positive  $x$ -axis. The visualisations of the instantaneous flow field for the three rudders at AOA  $10^\circ$ ,  $15^\circ$ ,  $20^\circ$ , and  $21.5^\circ$  can be seen in Figs. 11, 12, 13, and 15, respectively. The indexing notation for individual tubercle sections from the previous section is adopted here, too, with  $C_1$  to  $C_n$  and  $T_1$  to  $T_n$ , describing individual crests and troughs, respectively, where  $C_1$  and  $T_1$  are closest to the root of the rudder.

In the attached flow regime at AOA  $10^\circ$  (Fig. 11) the flow profiles of the TLE rudders are already much different to that of the SLE rudder. SLE (Fig. 11a) shows positive vorticity over the suction side that is indicative of the spanwise flow component inherent in finite-span foils. The spanwise flow forms an unstable vortex sheet behind the TE and subsequently rolls up into the tip vortex. In Area A of Fig. 11 it can be seen how positive vorticity is generated from the tip-facing tubercle side and negative vorticity from the root-facing side. This is the initial stream-wise counter-rotating vorticity resulting from the flow being diverted into the troughs and vorticity bending from a spanwise into the stream-wise direction around the individual tubercles. The circulation of these vortices increases with chordwise distance behind the troughs (see Fig. 11 Area A). The flow compartmentalisation over the rudder suction side due to the tubercle vortices can clearly be seen. It appears to be more pronounced for TLE7.

This may lead to a greater reduction in spanwise flow, which in turn reduces the induced drag and increases  $C_L$  as visible from the force coefficient results.

The small stall cells that form downstream from the troughs play a key role in the tubercle vortex pair formation. The stream-wise vortices are strengthened significantly on either side of these stall cells before they are shed into the wake (see Fig. 11 Area B). Studying the tubercle vortex formation on infinite-span hydrofoils, the strengthening mechanisms have been explained in detail by Hansen et al. (2016) and Rostamzadeh et al. (2014) for infinite-span foils. The observations from this study suggest that the principal vortex generating mechanism is the same in the case of a finite-span hydrofoil. The inherent spanwise flow component

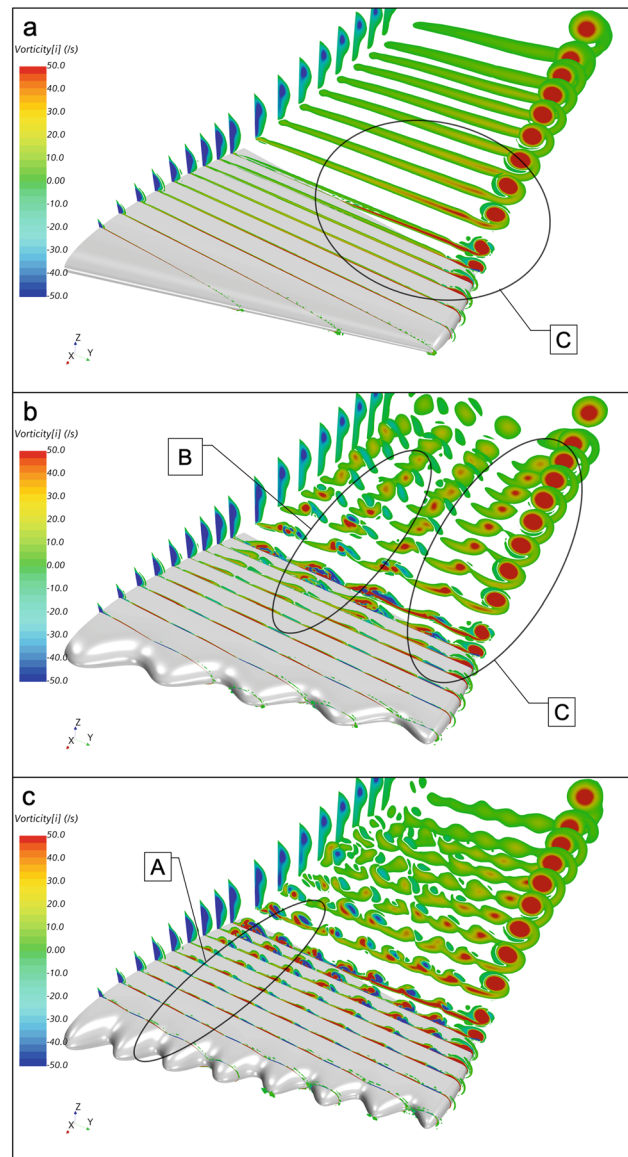


**Fig. 11** Isosurface visualisation of stream-wise vorticity for SLE (a), TLE4 (b), and TLE7 (c) at AOA  $10^\circ$

present for 3D foils, however, causes the tubercle vortices to be generated with unequal strength and size. This is due to the negative tubercle vortices opposing the primary spanwise flow direction, whereas the positive tubercle vortices are strengthened by it.

The tubercle vortices themselves strongly interact with each other, as can be seen in Fig. 11 Area B. The weaker negative vortex gets drawn into the strain field of the stronger positive one, begins circling around the positive one, and eventually merges. This effect is present for all tubercle vortex pairs. Still, it is more pronounced in the tip areas where, due to being strengthened by the stronger spanwise flow component, the positive tubercle vortices annihilate their negative counterparts a short distance downstream from the TE. The

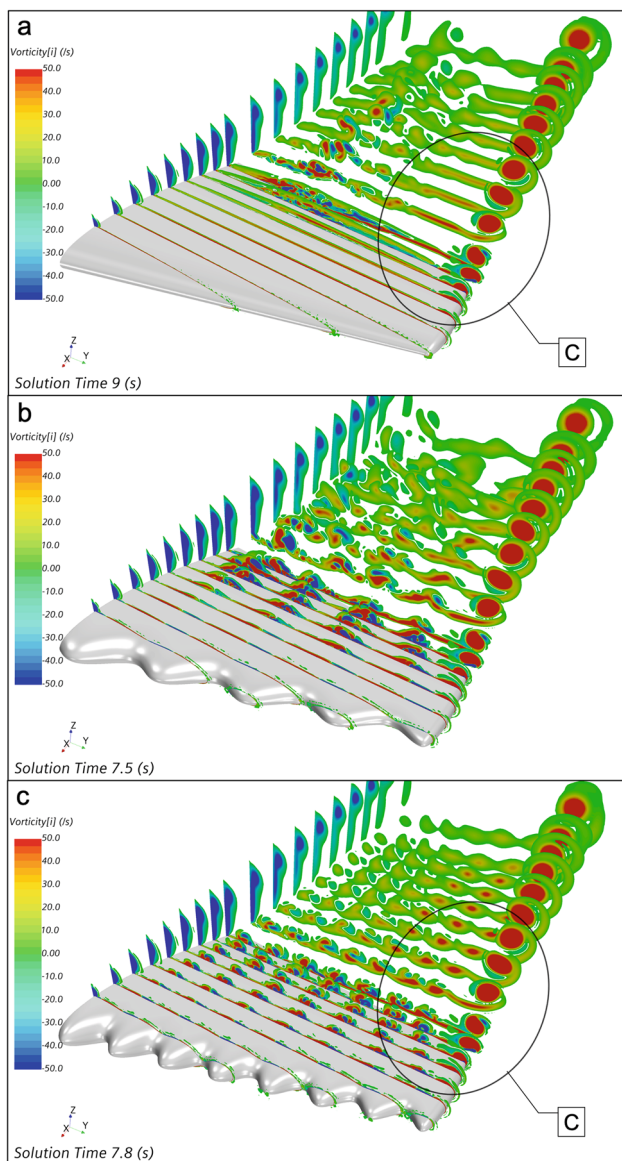


**Fig. 12** Isosurface visualisation of stream-wise vorticity for SLE (a), TLE4 (b), and TLE7 (c) at AOA 15°

positive tubercle vortices persist within the wake up to 2–3  $C_{nom}$  downstream from the TE and break up the trailing-edge vortex sheet. The strongest and most defined positive tubercle vortices are the ones located closest to the tip. They also experience the greatest influence from the tip vortex strain field, which slowly turns them towards the tip vortex with increasing distance downstream where they begin to merge (see Figs. 11 and 12 Area C).

#### 4.4 Changing of the flow separation behaviour through TLE application

The flow separation behaviour of the TLE rudders is very different to that of the reference rudder. The SLE rudder

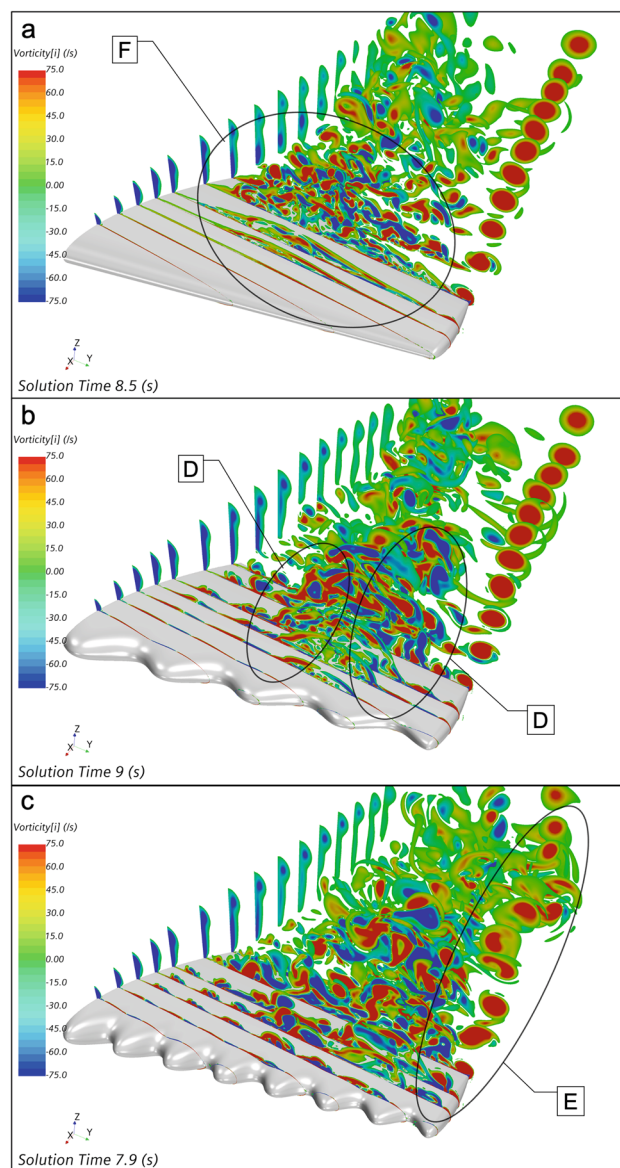


**Fig. 13** Isosurface visualisation of stream-wise vorticity for SLE (a), TLE4 (b), and TLE7 (c) at AOA 20°

shows an onset of flow separation centralised on the TE at AOA 15° (see Fig. 12a), which rapidly spreads out across the span and towards the LE as AOA is increased to 20° (see Fig. 13 Area F). For the TLE rudders, some of the small stall cells that form in the trough sections begin to combine as AOA is increased, but the flow compartmentalisation effect limits the general spread of flow separation. The flow over the crests remains largely attached. The TLE shifts the spanwise position of the separated flow areas. Flow separation on the SLE rudder occurs from 10 to 80% span. TLE4 confines it between the  $T_2$  and  $C_4$  from 40 to 75% span and TLE7 from  $T_4$ , or 52% span, outwards.

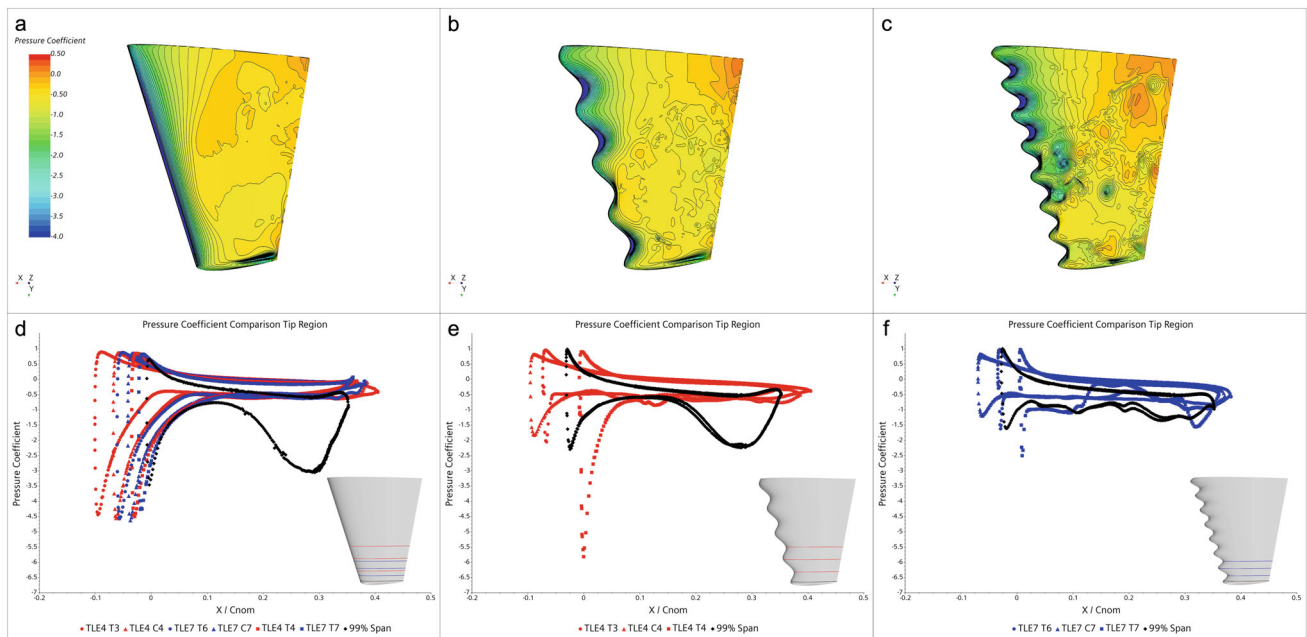


**Fig. 14** Pressure coefficient distribution comparison between SLE (a, d), TLE4 (b, e), and TLE7 (c, f) at AOA 20° for rudder suction side (top) and representative foil sections in the tip area (bottom), clearly highlighting the tip-unloading effect occurring for TLE7

Rostamzadeh et al. (2017) showed that, similarly to the localised stall cells of the tubercle troughs, large stream-wise vorticity of opposing sign forms on either side of the larger separation area of TLE foils when multiple stall cells combine. This effect is evident for TLE4 (see Area D in Fig. 13), as well as for the separation area of TLE7. The formation of a large negative vortex in the vicinity of the tip vortex induces elliptic flow in the tip vortex core, as well as first signs of long-wave Crow and/or elliptic instabilities that distort the vortex trajectory.

The most striking difference can be seen when comparing the tip vortices of SLE and TLE7. The tip vortex for the SLE has a coherent and well-developed vortex core with a straight trajectory. With most of the flow separation of TLE7 located in the tip region of the rudder, a “tip-unloading effect” occurs, which has a strong impact on the tip vortex. It is heavily distorted, showing signs of elliptic flow within the core, diffusion, as well as potential long-wave instabilities in its path (see Figs. 13 and 15 Area E). Due to the flow being largely separated near the tip, the pressure imbalances between the rudder pressure and suction side is smaller, causing less flow to spill over the rudder tip and generating a weaker tip vortex. This tip vortex is then further destabilised by the negative stream-wise vortex elements forming around the stall cell.

The tip-unloading effect is clear when comparing the pressure coefficients over the rudder suction side and the representative foil sections in the tip area, as presented in Fig. 14. The pressure coefficient distribution over the surface of the SLE rudder shows how the flow is only attached

for 1/4–1/3 of the chord from the leading edge, and separation has spread out across the entire rudder span (see Fig. 14a). Still, a significant proportion of lift is generated in the tip region as indicated by the large low-pressure peak visible for the pressure coefficient distributions plotted over the selected tip chords in Fig. 14d. Figure 14b shows how the flow separation for TLE4 is confined between  $T_2$  and  $T_4$ , whilst the flow is largely attached in the root area and to an extent over the tip. The representative crest and trough sections in the tip area of TLE4 still show the typical pressure coefficient profiles for TLE rudders discussed in Sect. 4.2 (see Fig. 14e). In Fig. 14c it can be seen how for TLE7 the flow detaches right at the LE in the tip area between  $C_6$  and  $C_7$  and there is very little flow attachment over the tip itself. This is also reflected in Fig. 14f where the tubercle trough section shows an unusually small low-pressure peak. The net pressure difference for all four sections plotted is much lower than the SLE and TLE4 rudders. Hence, very little lift is generated in this area of the rudder giving rise to the tip-unloading effect.

The results indicate a correlation between tubercle wavelength and/or the number of tubercles and the spanwise positioning of stall onset. The shorter wavelength and larger number of tubercles have shifted the flow separation area towards the rudder tip. This effect needs to be verified through tests of additional geometry configurations.

As the flow in the root area is closer to being two-dimensional than in the tip area, the tubercle vortices are generated at equal strength and do not cancel each other out. As a result, they energise the boundary layer, and the flow

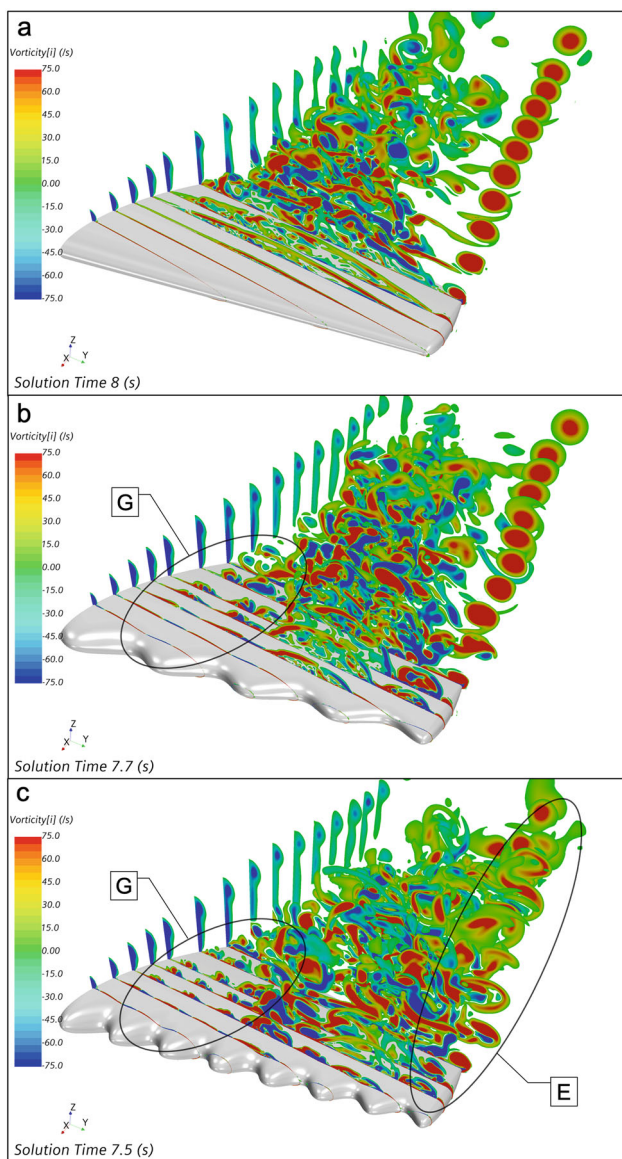


**Fig. 15** Isosurface visualisation of stream-wise vorticity for SLE (a), TLE4 (b), and TLE7 (c) at AOA 21.5°

remains attached for almost the entire chord length, as can be seen in Fig. 15 Area G. It is at these higher AOA when the SLE rudder stalls that the TLE rudders display the large increases in  $C_L$  as they can maintain flow attachment for at least part of the suction side surface.

### 4.5 Turbulent kinetic energy within the downstream wake and tip vortex decay

Sections 4.3 and 4.4 have highlighted the very different flow profiles caused by the TLE, how the tubercle vortices alter the turbulent wake of a typical finite-span hydrofoil and how they, directly and indirectly, influence the tip vortex. To better understand the full turbulent wake of the different rudders,

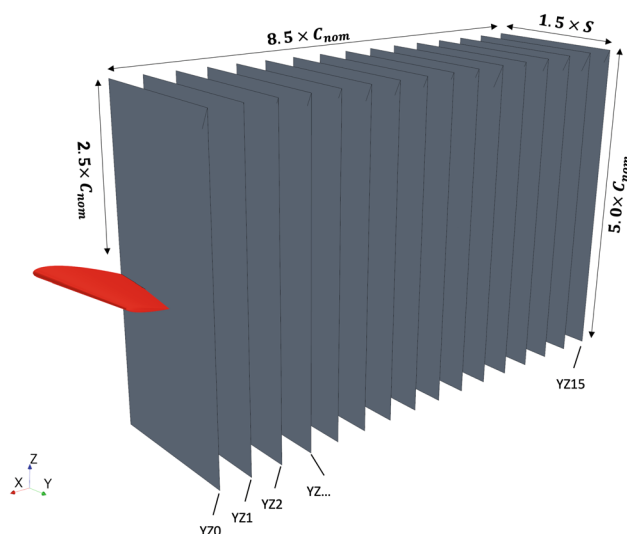


**Fig. 16** Vertical cut planes in the downstream wake area at intervals from the trailing edge to calculate wake performance metrics

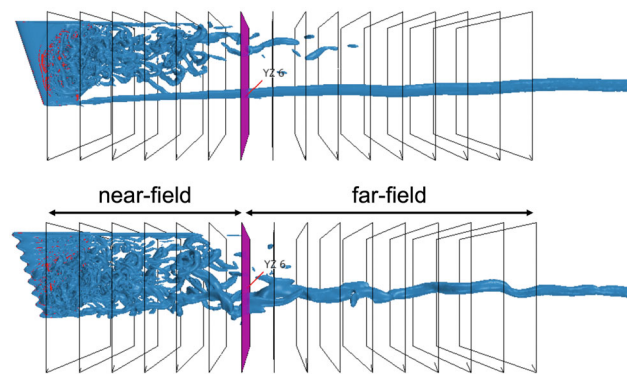


**Fig. 17** Breakdown of downstream wake area into near-field and far-field wake

further analysis methods were employed. The vortical wake structures were visualised using Q-criterion iso-surface with  $Q = 100.0/s^2$ . 16 vertical cut planes were added to the downstream wake area at evenly spaced intervals up to 8.5 chord lengths distance from the TE, as shown in Fig. 16. To quantify the strength of the wake, the mean and peak turbulent kinetic energy was recorded at each plane section and averaged over a 0.5s time interval.

The wake itself can be separated into a near-field and far-field wake region, as outlined in Fig. 17. The near-field wake describes the area dominated by the chaotic flow structures caused by the separated boundary layer, which for most cases decayed within 3 chord lengths downstream around station YZ6. From station YZ6 onwards, the tip vortex becomes the main flow feature that dictates the TKE levels. Additionally, the TKE was displaced on the Q-criterion isosurfaces to give a better insight into where the high and low energy areas of the wake are located.

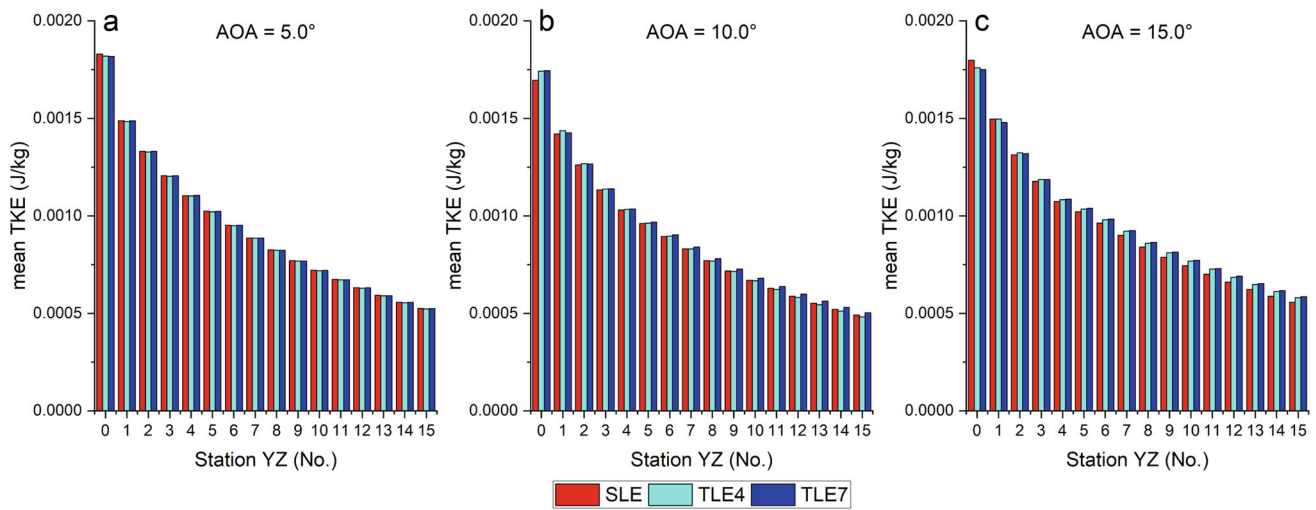


**Fig. 18** Mean turbulent kinetic energy levels at vertical cut planes downstream from the trailing edge for AOA 5°, 10°, and 15°

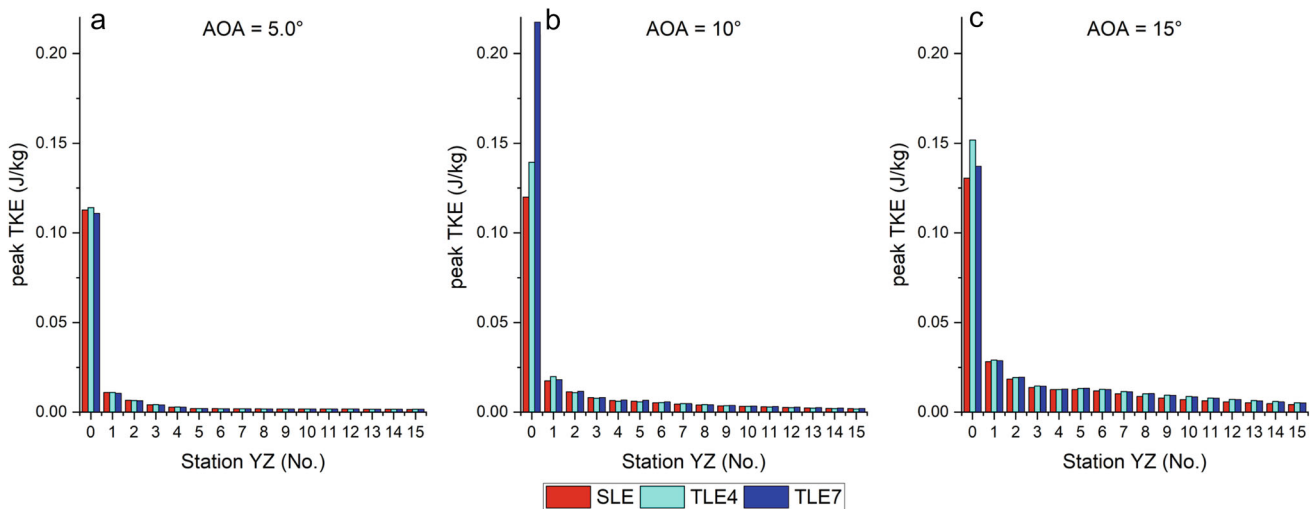


**Fig. 19** Average peak turbulent kinetic energy levels at vertical cut planes downstream from the trailing edge for AOA 5°, 10°, and 15°

Figure 18 shows the mean TKE data for the pre-stall regime. It can be seen how at AOA 5° all three rudders perform nearly identical. There is a minimal reduction in TKE for stations 0 and 1, potentially due to the early formation of tubercle vortices breaking up the trailing-edge vortex sheet. For AOA 10°, the TLE rudders show a small increase in TKE for stations 0 and 1 due to the local stall cells in the troughs forming small, separated wakes that dissipate energy, whilst the flow for the SLE rudder is still fully attached (recall Fig. 11). This is highlighted by the peak TKE values in Fig. 19b, which are significantly higher for TLE7 which at this angle forms stronger tubercle vortices, leading to a stronger initial wake but also more lift. The far-field results in Fig. 18b agree with the lifting behaviour of the rudders

as TLE7 increased lift compared to SLE at this angle, therefore generating a stronger tip vortex, with the opposite effect shown for TLE4, which reduced lift.

The effects of the TLE change for AOA 15° when the SLE rudder starts showing first signs of flow separation. The numerous, smaller separation cells of the TLE, on average, generate less TKE compared to the separated flow area spanning across the trailing edge of the SLE rudder (see Fig. 18c Stations 0/1). The small separation cells themselves, however, show higher peak TKE values (see Fig. 18c Station 0). This can also be seen comparing the wake in the close vicinity of the rudders in Fig. 20, which highlights the spread-out separation for SLE and the numerous energetic stall cells in the case of TLE7. The figure also shows how the tubercle vortex pairs break up the trailing-edge vortex sheet, which may

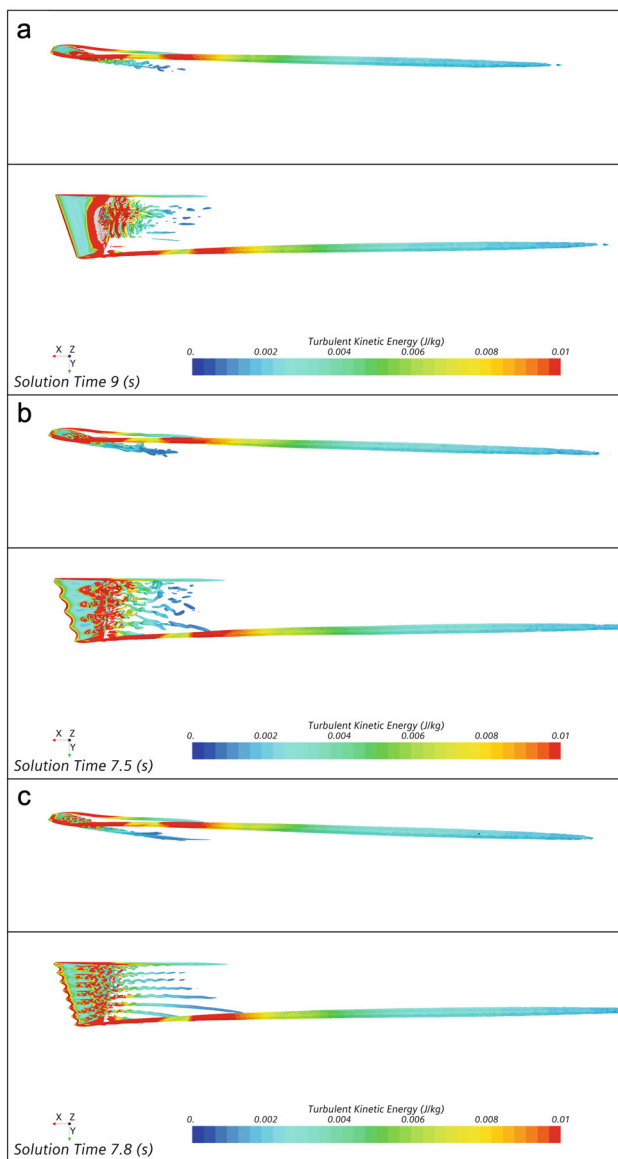


**Fig. 20** Turbulent kinetic energy visualised on Q-criterion iso-surface for SLE (a), TLE4 (b), and TLE7 (c) at AOA 15°

have contributed to the reduction in mean TKE in the near field. In the far-field the TLE rudders show slightly higher TKE values due to the increased lift that they generate.

At the onset of flow stall at AOA 20° and 21.5° significant differences can be observed. At AOA 20° the SLE rudder develops a strong coherent tip vortex that streams in a straight line (Fig. 21a). For TLE4, the larger vortical elements generated around the separation area remain persistent within the turbulent wake and begin interacting with the tip vortex several chord lengths downstream. The stronger co-rotating tip vortex core causes these elements to circulate around it, where they merge and dissipate. In the process the tip vortex begins to show long-wave instabilities, clearly visible in

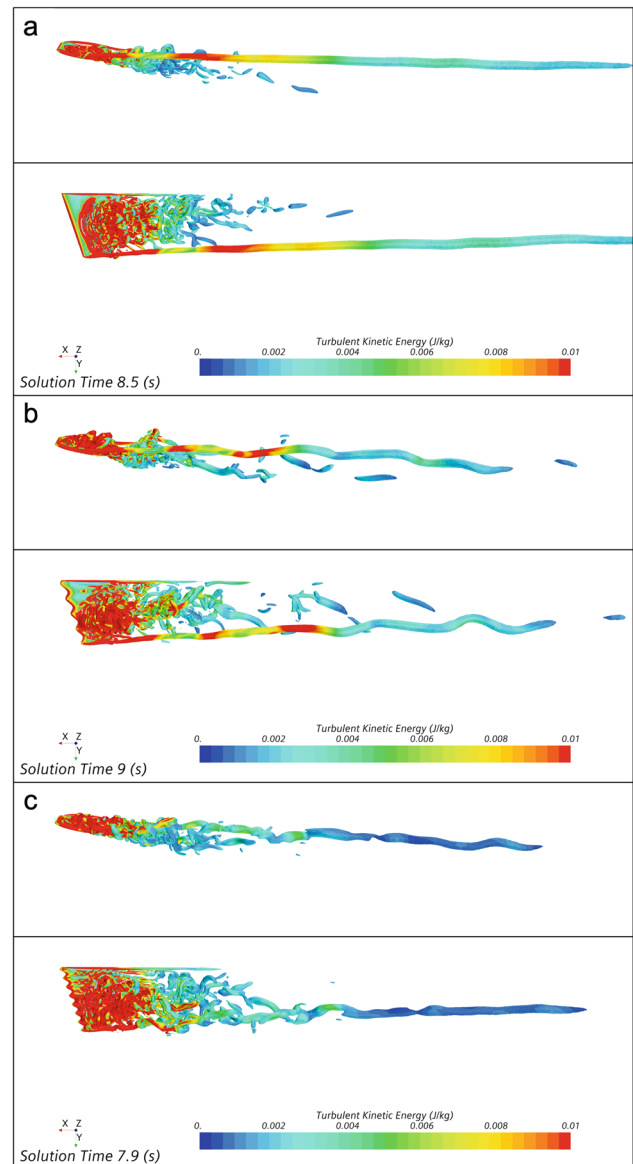


**Fig. 21** Turbulent kinetic energy visualised on Q-criterion iso-surface for SLE (a), TLE4 (b), and TLE7 (c) at AOA 20°

the vertical plane. These long-wave instabilities accelerate its decay, as can be seen in Fig. 21b.

Figure 21c highlights the impact the tip-unloading has on the tip vortex generated by TLE7. The larger negative vortical structure forming around the stall cell is located close to the tip vortex inducing long-wave Crow instabilities immediately. The initially weakened tip vortex experiences a second interaction with the positive, co-rotating vortex generated around the root side of the stall cell, approximately 2 chord lengths downstream. The difference in the strength of these two vortices is smaller, causing them to merge in a spiralling motion further weakening the tip vortex. Out of the three rudders, TLE7 has the fastest tip vortex dissipation.

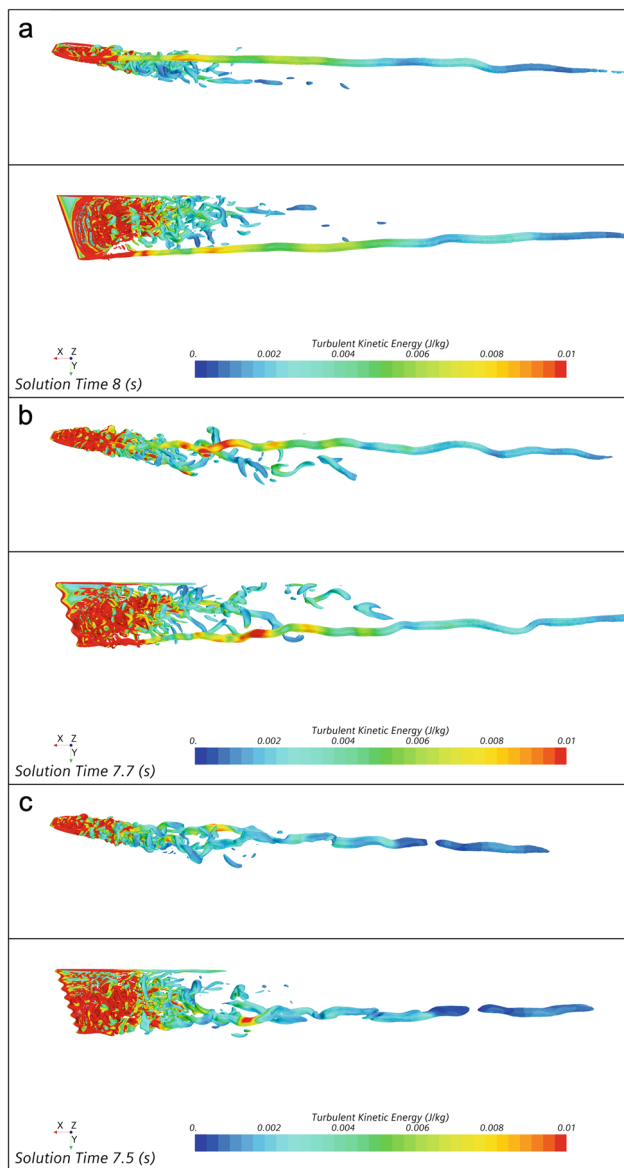


**Fig. 22** Turbulent kinetic energy visualised on Q-criterion iso-surface for SLE (a), TLE4 (b), and TLE7 (c) at AOA 21.5°

The effect discussed above is evident when comparing the mean and peak TKE levels in the far-field of the rudders. Figure 21a shows how TLE7 reduces the mean TKE for all stations downstream of Station 5 by up to 11% whilst producing 3% more lift. This highlights the destabilisation of the tip vortex. The TKE levels for TLE4 are higher or matched to the SLE rudder in the near and far fields as the rudder produces more lift but does not experience tip-unloading.

In the near field, both TLE rudders show higher mean and peak TKE levels. This is due to the size of the separated wake from the TLE. Whilst the tubercle vortices confine the spanwise spread of the separation, the separated wake itself appears to be larger and more energetic, as seen in the side

view in Fig. 21b, c. This large, separated wake also causes the drag penalty for the TLE rudders at the higher AOA.

At AOA 21.5°, the SLE rudder is stalled, and it can be seen how the flow separation has moved all the way forward to the LE (see Fig. 22a). The SLE rudder now also shows a large separation wake, and its near-field TKE levels are similar to the TLE rudders'. Still, a fully developed tip vortex is generated. The different flow dynamics the TLE rudders displayed for AOA 20° continue for AOA 21.5°. TLE4 shows a large near-field wake with distinct vortical elements that introduce long-wave elliptical and/or Crow instabilities into the tip vortex core (see Fig. 22b). TLE7 fails to form a coherent tip vortex. The vortex that is generated is low in energy, skewed, fragmented and decays quickly (see Fig. 22c). The weaker vortex core of TLE7 appears to be larger in diameter, which can be an additional sign of diffusion.

Comparing the mean TKE levels of the three rudders at AOA 21.5° in Fig. 24c some interesting observations can be made. In the near field, the TLE rudders show slightly higher energy levels due to the larger separated wake again. In the far field, where the tip vortex dominates, TLE4 shows the highest TKE levels. The levels for TLE7 are matched with those of the SLE rudder or lower. An increase in TKE would be expected as TLE4, and TLE7 generate 4.5% and 7.5% more lift respectively, however, this is only the case for TLE4. Despite producing significantly more lift, the tip-unloading effect of TLE7, paired with the interaction of the tubercle vortices, diffuses the tip vortex and accelerates its decay.

In Fig. 23 for post-stall AOA 25° the wake dynamics of the rudders show several differences. SLE and TLE4 still form a clearly distinguishable tip vortex, whereas TLE7 shows a larger near-field wake with fragmented tip vortex elements being shed downstream. The flow of all three rudders detaches a short distance from the LE, and large separation wakes form with very similar mean TKE levels (see Fig. 24c). The peak TKE levels of the near field in Fig. 25c are the highest for TLE4 at Station 0. However, these results are to be treated with care, as the simulations at these high AOA become very unstable, with large wake elements being shed as the flow separates and reattaches from the rudder surface.

Whilst the TLE modifications in this study may not have improved the efficiency of the reference rudder, many important observations were made of how the stream-wise counter-rotating vortex pairs generated by the tubercles drastically change the wake flow dynamics. The compartmentalisation of the flow over the rudder suction side surface that was shown altered the separation behaviour, which led to several carry-on effects. The most notable being the tip-unloading effect from TLE7, which caused a rapid diffusion of the tip vortex whilst maintaining lifting performance. Generally, there appears to be a trade-off for the TLE modifications between a slight increase in near-field wake size

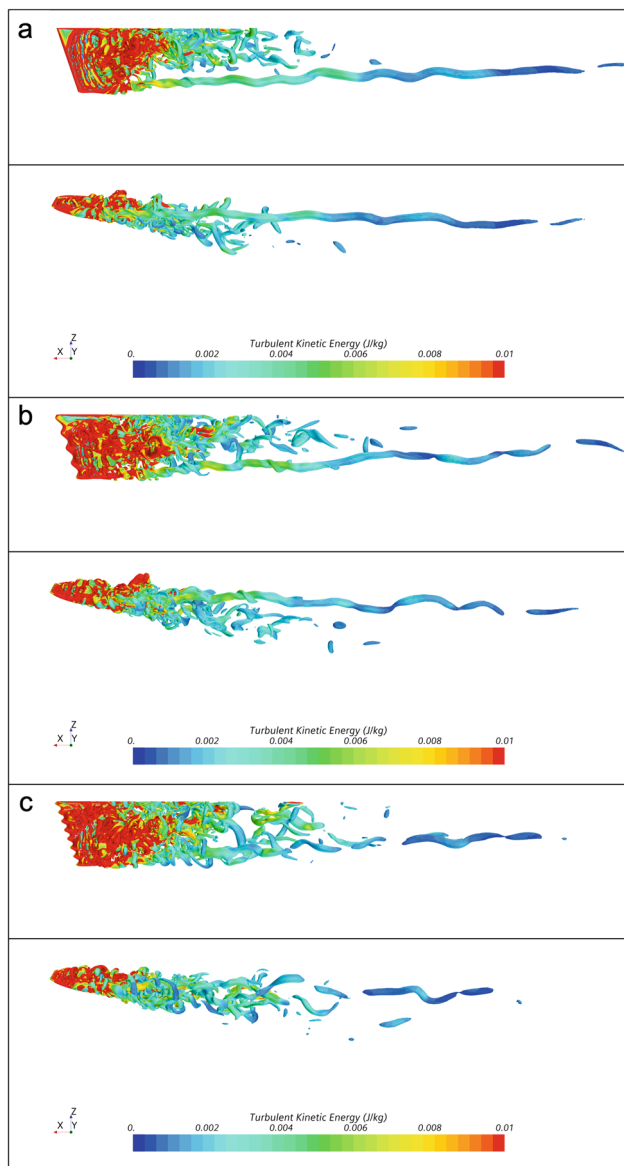


**Fig. 23** Turbulent kinetic energy visualised on Q-criterion iso-surface for SLE (a), TLE4 (b), and TLE7 (c) at AOA 25.0°

and energy against a weakening of the far-field wake and accelerating its decay.

## 5 Conclusion

A representative marine rudder and two tubercle leading-edge modifications were analysed numerically using DES. The three models were simulated for a fully turbulent Reynolds number of  $2.26 \times 10^6$  over eight angles of attack ranging from 0° to 30°. The numerical model was validated via force coefficient comparisons, which were subsequently

used to evaluate the lifting performance of the individual rudders. However, the main body of the study focussed on the changes in the flow dynamics over the rudder surface and within the turbulent wake downstream from the rudder that were induced by the tubercle modifications. Particular focus was devoted to the tip vortex, which is the most distinct feature of the rudder wake. The results presented in this study discussed analyses of flow visualisations via iso-surface, and turbulent kinetic energy measurements in the downstream wake. The wake flow dynamics of the two TLE rudders were inherently different to those of the SLE reference rudder. The following conclusions can be drawn:

1. The TLE rudders enhanced lift all AOA above 10° with the most significant improvements in the post-stall regime, making the rudders more effective. The tubercles caused an increase in drag, thereby reducing the rudder efficiency slightly.
2. The formation of stream-wise counter-rotating vortex pairs behind the tubercles was shown. Span-wise flow effects caused the vortices generated to be of unequal strength and the negative vortices to be annihilated by their positive counterparts. The positive tubercle vortices remained persistent within the flow up to  $3 C_{nom}$  downstream from the TE, breaking up the vortex sheet and subsequent tip vortex roll-up.
3. At higher AOA, the TLE modifications changed the flow separation on the rudder suction side through flow compartmentalisation. Separation for the SLE rudder began centralised on the TE and spread out across the entire span. TLE4 confined flow separation centralised between tubercles  $T_2$  and  $C_4$ . TLE7 confined separation outwards from  $T_4$ . It appeared that a larger number of tubercle vortices improves the flow compartmentalisation and shifts the flow separation onset towards the rudder tip.
4. The shift in flow separation resulted in a “tip-unloading effect” for TLE7. Lift generation in the tip area was reduced which weakened the initial formation of the tip vortex significantly, diffused it and accelerated the decay downstream. This reduced the TKE levels in the far-field wake area despite the rudder increasing lift.
5. Vortical elements of counter-rotating vorticity were generated on either side of the separation area of each TLE rudder. Interaction of this vorticity with the tip vortex had weakening effects, causing long-wave instabilities and displacing the tip vortex in its trajectory.

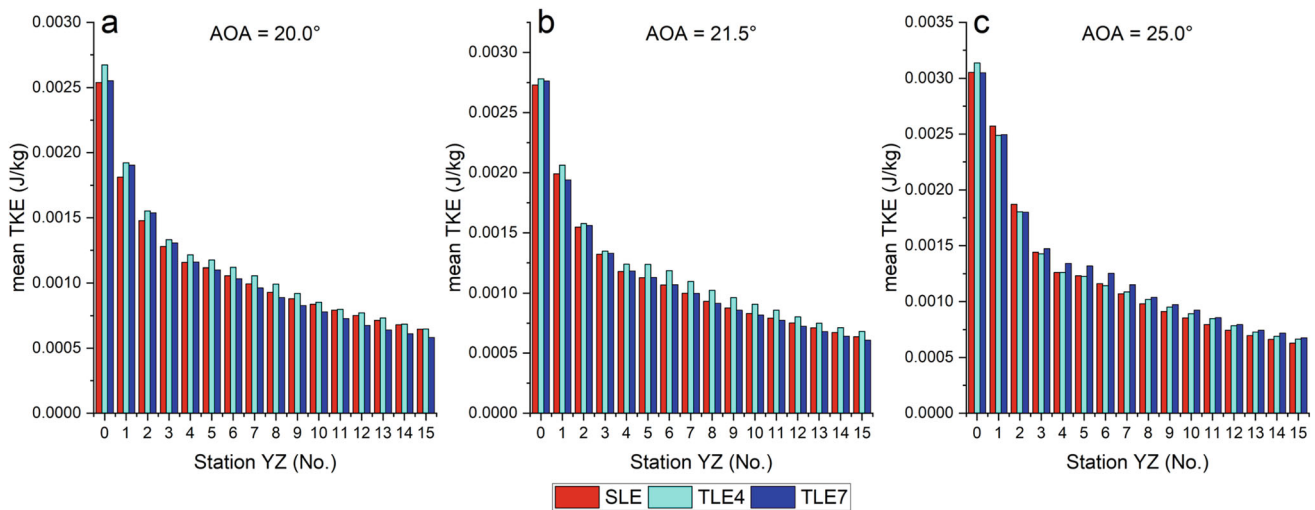


**Fig. 24** Mean turbulent kinetic energy levels at vertical cut planes downstream from the trailing edge for AOA 20°, 21.5°, and 25°

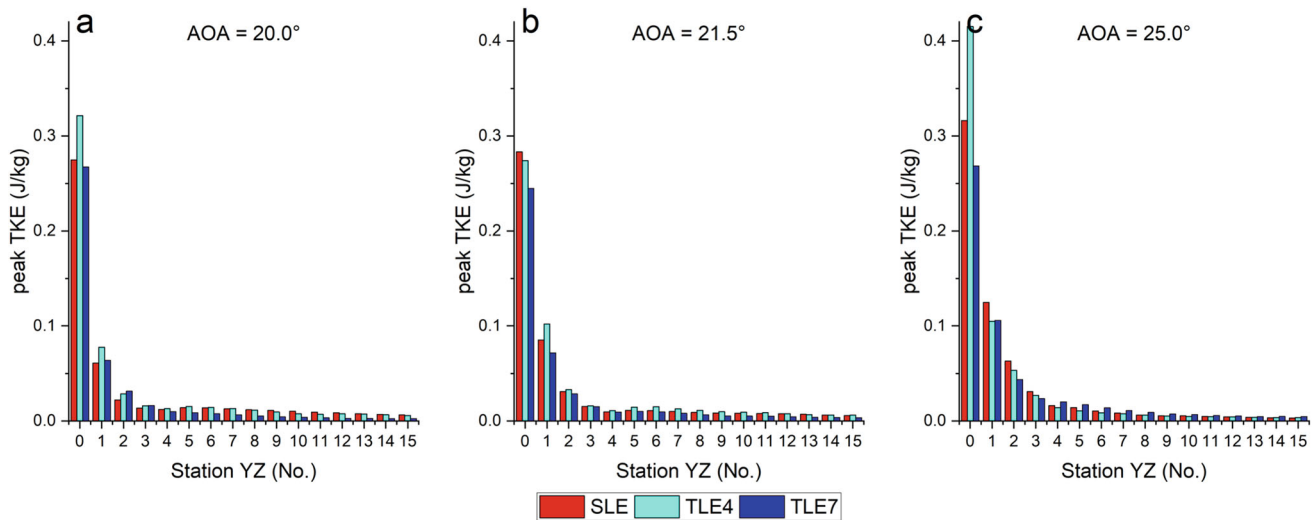


**Fig. 25** Average peak turbulent kinetic energy levels at vertical cut planes downstream from the trailing edge for AOA 20°, 21.5°, and 25°

**Acknowledgements** The results were obtained using the University of Strathclyde's High Performance Computer ARCHIE-WeSt (<https://www.archie-west.ac.uk/>). This work was supported BAE systems plc. (Ref: MEIR PhD 17), which is greatly appreciated and acknowledged.

**Funding** This work was funded by BAE systems plc. (Ref: MEIR PhD 17).

**Open Access** This article is licensed under a Creative Commons Attribution 4.0 International License, which permits use, sharing, adaptation, distribution and reproduction in any medium or format, as long as you give appropriate credit to the original author(s) and the source, provide a link to the Creative Commons licence, and indicate if changes were made. The images or other third party material in this article are included in the article's Creative Commons licence, unless indicated otherwise in a credit line to the material. If material is not included in the article's Creative Commons licence and your intended use is not permitted by statutory regulation or exceeds the

permitted use, you will need to obtain permission directly from the copyright holder. To view a copy of this licence, visit <http://creativecommons.org/licenses/by/4.0/>.

## References

- Bolzon MD, Kelso RM, Arjomandi M (2015) Tubercles and their applications. *J Aerosp Eng* 29:1–10. [https://doi.org/10.1061/\(ASCE\)AS.1943-5525](https://doi.org/10.1061/(ASCE)AS.1943-5525)
- Bolzon MD, Kelso RM, Arjomandi M (2017) Performance effects of a single tubercle terminating at a swept wing's tip. *Exp Therm Fluid Sci* 85:52–68. <https://doi.org/10.1016/j.expthermflusci.2017.02.016>
- Câmara JFD, Sousa JMM (2013) Numerical study on the use of a sinusoidal leading edge for passive stall control at low Reynolds number. In: 51st AIAA aerospace sciences meeting including the new horizons forum and aerospace exposition 2013. American

- Institute of Aeronautics and Astronautics, Dallas. <https://doi.org/10.2514/6.2013-62>
- Carrica PM, Kim Y, Martin JE (2019) Near-surface self propulsion of a generic submarine in calm water and waves. *Ocean Eng* 183:87–105. <https://doi.org/10.1016/j.oceaneng.2019.04.082>
- Celik IB, Ghia U, Roache PJ, Freitas CJ, Coleman H, Raad PE (2008) Procedure for estimation and reporting of uncertainty due to discretization in CFD applications. *J Fluids Eng Trans ASME*. <https://doi.org/10.1115/1.2960953>
- Custodio D (2012) The Effect of Humpback Whale-Like Leading Edge Protuberances. Worcester Polytechnic Institute.
- Custodio D, Henoach CW, Johari H (2015) Aerodynamic characteristics of finite span wings with leading-edge protuberances. *AIAA J*. <https://doi.org/10.2514/1.J053568>
- Fish FE, Battle JM (1995) Hydrodynamic design of the humpback whale flipper. *J Morphol* 225:51–60. <https://doi.org/10.1002/jmor.1052250105>
- Fish FE, Howle LE, Murray MM (2008) Hydrodynamic flow control in marine mammals. *Integr Comp Biol*. <https://doi.org/10.1093/icb/1.029>
- Folger Whicker L, Fehlner LF (1958) Free-stream characteristics of a family of low-aspect-ratio, all-movable control surfaces for application to ship design, Washington, D.C.
- Hansen KL, Rostamzadeh N, Kelso RM, Dally BB (2016) Evolution of the streamwise vortices generated between leading edge tubercles. *J Fluid Mech* 788:730–766. <https://doi.org/10.1017/jfm.2015.611>
- Johari H (2015) Cavitation on hydrofoils with sinusoidal leading edge. In: *Journal of physics: conference series—9th international symposium on cavitation (CAV2015)*. IOP Publishing, Lausanne. <https://doi.org/10.1088/1742-6596/656/1/012155>
- Knister D, Callison E, Ganesh H, Ceccio SL, Arbor A (2020) Experimental study of cavitation inception during the interaction of vortices. In: *33rd symposium on naval hydrodynamics*, Osaka
- Leweke T, Le Dizès S, Williamson CHK (2016) Dynamics and instabilities of vortex pairs. *Annu Rev Fluid Mech* 48:507–541. <https://doi.org/10.1146/annurev-fluid-122414-034558>
- Liu J, Hekkenberg R (2017) Sixty years of research on ship rudders: effects of design choices on rudder performance. *Ships Offshore Struct* 12:495–512. <https://doi.org/10.1080/17445302.2016.1178205>
- Loughnane F, Mongin M, Gunasekaran S (2021) Effect of airfoil-preserved undulation placement on wing performance and wingtip vortex. *AIAA J* 59:1598–1613. <https://doi.org/10.2514/1.j059517>
- Malipeddi AK, Mahmoudnejad N, Hoffmann KA (2012) Numerical analysis of effects of leading-edge protuberances on aircraft wing performance. *J Aircr* 49:1336–1344. <https://doi.org/10.2514/1.C031670>
- Miklosovic DS, Murray MM, Howle LE, Fish FE (2004) Leading-edge tubercles delay stall on humpback whale (*Megaptera novaeangliae*) flippers. *Phys Fluids* 16:L39–L42. <https://doi.org/10.1063/1.1688341>
- Miklosovic DS, Murray MM, Howle LE (2007) Experimental evaluation of sinusoidal leading edges. *J Aircr* 44:1404–1408. <https://doi.org/10.2514/1.30303>
- Molland AF, Turnock SR (2007) *Marine rudders and control surfaces: principles, data, design and applications*. Elsevier/Butterworth-Heinemann, Oxford
- Pedro HTC, Kobayashi MH (2008) Numerical Study of stall delay on humpback whale Flippers. In: *46th AIAA aerospace sciences meeting and exhibit*. American Institute of Aeronautics and Astronautics, Reno. <https://doi.org/10.2514/6.2008-584>
- Rostamzadeh N, Hansen KL, Kelso RM, Dally BB (2014) The formation mechanism and impact of streamwise vortices on NACA 0021 airfoil's performance with undulating leading edge modification. *Phys Fluids* 26:1–22. <https://doi.org/10.1063/1.4896748>
- Rostamzadeh N, Kelso RM, Dally B (2017) A numerical investigation into the effects of Reynolds number on the flow mechanism induced by a tubercled leading edge. *Theor Comput Fluid Dyn*. <https://doi.org/10.1007/s00162-016-0393-x>
- Shanmukha Srinivas K, Datta A, Bhattacharyya A, Kumar S (2018) Free-stream characteristics of bio-inspired marine rudders with different leading-edge configurations. *Ocean Eng* 170:148–159. <https://doi.org/10.1016/j.oceaneng.2018.10.010>
- Shi W, Atlar M, Norman R, Aktas B, Turkmen S (2016) Numerical optimization and experimental validation for a tidal turbine blade with leading-edge tubercles. *Renew Energy* 96:42–55. <https://doi.org/10.1016/j.renene.2016.04.064>
- Spalart PR (2001) *Young-person's guide to detached-eddy simulation grids*, Hampton
- Stanway MJ (2008) Hydrodynamic effects of leading-edge tubercles on control surfaces and in flapping foil propulsion. Massachusetts Institute of Technology
- Stark C, Shi W (2021) The influence of leading-edge tubercles on the hydrodynamic performance and propeller wake flow development of a ducted propeller. In: *31st international ocean and polar engineering conference*, Rhodes
- Stark C, Shi W, Troll M (2021) Cavitation funnel effect: Bio-inspired leading-edge tubercle application on ducted marine propeller blades. *Appl Ocean Res* 116:102864. <https://doi.org/10.1016/j.apor.2021.102864>
- Weber PW, Howle LE, Murray MM (2010) Lift, drag, and cavitation onset on rudders with leading-edge tubercles. *Mar Technol* 47:27–36. <https://doi.org/10.5957/mtsn.2010.47.1.27>
- Yoon HS, Hung PA, Jung JH, Kim MC (2011) Effect of the wavy leading edge on hydrodynamic characteristics for flow around low aspect ratio wing. *Comput Fluids*. <https://doi.org/10.1016/j.compfluid.2011.06.010>

**Publisher's Note** Springer Nature remains neutral with regard to jurisdictional claims in published maps and institutional affiliations.